AIP | Journal of Applied Physics

# Pressure-induced ferroelectric to paraelectric transition in LiTaO3 and (Li,Mg)TaO3

Takamitsu Yamanaka, Yuki Nakamoto, Fumihiko Takei, Muhtar Ahart, Ho-kwang Mao, and Russell J. Hemley

Citation: Journal of Applied Physics **119**, 075902 (2016); doi: 10.1063/1.4941383
View online: http://dx.doi.org/10.1063/1.4941383
View Table of Contents: http://scitation.aip.org/content/aip/journal/jap/119/7?ver=pdfcov
Published by the AIP Publishing

---

---

JOURNAL OF APPLIED PHYSICS **119**, 075902 (2016)

HPSTAR
236-2016

# Pressure-induced ferroelectric to paraelectric transition in $LiTaO_3$ and $(Li,Mg)TaO_3$

Takamitsu Yamanaka,[1,a)] Yuki Nakamoto,[2] Fumihiko Takei,[3] Muhtar Ahart,[1] Ho-kwang Mao,[1,4] and Russell J. Hemley[1,b)]
[1]*Geophysical Laboratory, Carnegie Institution of Washington, Washington, DC, 20015, USA*
[2]*KYOKUGEN, Graduate School of Engineering Science, Osaka University, Osaka, Japan*
[3]*Graduate School of Science, Osaka University, Osaka 560-8531, Japan*
[4]*Center for High Pressure Science and Technology Advanced Research, Shanghai 201203, China*

(Received 27 August 2015; accepted 22 January 2016; published online 16 February 2016)

X-ray powder diffraction and Raman scattering of $LiTaO_3$ (LT) and $(Li,Mg)TaO_3$ (LMT) have been measured under pressure up to 46 GPa. Above 30 GPa, the ferroelectric rhombohedral phase ($R3c$, $Z = 6$) of $LiTaO_3$ transforms to a paraelectric orthorhombic phase ($Pnma$ with $Z = 4$) with a large hysteresis. Rietveld profile fitting analysis shows that the Li-O bond is compressed and approaches that of Ta-O with pressure. The cation distribution analysis of the orthorhombic perovskite structure shows that Li and Ta are located in the octahedral 8-fold coordination sites. Difference Fourier $|F_{obs}(hkl)|$ - $|F_{cal}(hkl)|$ maps of $LiTaO_3$ and $(Li,Mg)TaO_3$ indicate polarization in the $c$ axis direction and a more distinct electron density distribution around the Ta position for $(Li,Mg)TaO_3$ compared to $LiTaO_3$. The observed effective charges indicate that for $(Li,Mg)TaO_3$ without vacancies $Ta^{5+}$ becomes less ionized as a function of Mg substitution. Considering both site occupancy and effective charge analysis, $Ta^{5+}$ is reduced to $Ta^{4.13+}$. $Mg^{2+}$ and $O^{2-}$ change to $Mg^{1.643+}$ and $O^{1.732-}$, respectively. The space- and time-averaged structures of the dynamical vibration of atoms can be elucidated from the electron density analysis by difference Fourier and temperature factors $T(hkl)$ in the structure refinement. The refinement of the temperature factor is consistent with the cation distribution assuming full stoichiometry. The residual electron density induced from the excess electron in $(Li,Mg)TaO_3$ indicates more electrons around the Ta site, as confirmed by the effective charge analysis. Raman spectra of $LiTaO_3$ and $(Li,Mg)TaO_3$ show notable changes over the measured pressure range. Raman peaks centered at 250 $cm^{-1}$ and 350 $cm^{-1}$ at ambient pressure merge above 8 GPa, which we associate with the diminishing of difference in distances between Li-O and Ta-O bonds with pressure in both materials. Raman spectra show significant changes at 28 GPa and 33 GPa for LT and LMT, respectively, due to the structural transition from $R3c$ to $Pnma$ consistent with the x-ray diffraction results.
[http://dx.doi.org/10.1063/1.4941383]

## I. INTRODUCTION

$LiTaO_3$ is an important optical material with excellent photorefractive, nonlinear, and electro-optic effects, ferroelectric and piezoelectric devices. The ferroelectric bulk crystals are widely used in optoelectronic devices. Indeed, along with $LiNbO_3$ and $KNbO_3$, $LiTaO_3$ is among the most important lead-free $A^{+}B^{5+}O_3$ ferroelectric materials. $LiTaO_3$ determined by x-ray[1–3] and neutron[4–6] diffraction has a $LiNbO_3$-type rhombohedral $R3c$ structure, where Li and Ta atoms are displaced from the center of octahedral along the trigonal $c$ axis, which induces the ferroelectric properties. Dielectric, thermal, and pyroelectric properties of ferroelectric $LiTaO_3$ have been investigated,[7] and many structures of the Curie temperature of the stoichiometric $LiTaO_3$, as well as $LiNbO_3$, have been reported (e.g., Refs. 8 and 9). The Curie temperature $T_c$ of $LiTaO_3$ (917–948 K) is much lower than that of $LiNbO_3$ (1475–1486 K). It has also been reported that the high temperature paraelectric phase is rhombohedral but has a centrosymmetric space group $R\,\bar{3}c$. Moreover, the elastic properties, dielectric susceptibilities, and electrical conductivity of $LiTaO_3$ have been measured over a broad temperature range up to 1200 K.[10] An order-disorder model for the oxygen atoms has been proposed as the driving mechanism for the ferroelectric instability and a large hybridization between the oxygen and the transition-metal atoms.[11] It has also been shown that the physical properties of $LiTaO_3$ and the solid solution $(Li,Mg)TaO_3$ are sensitive to the existence of intrinsic and extrinsic defects.[7,11–13] The transition temperature $T_c$ depends on doping by Mg.[14] Indeed, the effect of Mg substitution on the electrical conductivity is an important topic for understanding ferroelectricity in $LiTaO_3$ based materials.[15]

High-pressure behavior of $LiTaO_3$ has also been investigated by x-ray diffraction and Raman scattering.[13,16] In order to gain further insight into these materials, we examine the effect of pressure on the structure of $LiTaO_3$ (LT) and $(Li,Mg)TaO_3$ (LMT) from ferroelectric rhombohedral phase ($R3c$, $Z = 6$) to the paraelectric orthorhombic perovskite phase ($Pnma$, $Z = 4$). In order to further understand the driving force of the transition, dynamical atomic thermal

---

[a)]E-mail: tyamanaka@ciw.edu
[b)]E-mail: rhemley@carnegiescience.edu

vibration is examined on compression and decompression. A charge transfer model of cations is used to interpret the mechanism of substitution of $Mg^{2+}$ in LMT, and the effective charges of the cations are analyzed using the electron densities determined by the x-ray diffraction refinements.

TABLE I. Structure of $LiTaO_3$ and $(Li,Mg)TaO_3$ at ambient conditions from single-crystal x-ray diffraction.

| | | $LiTaO_3$ | | $(Li,Mg)TaO_3$ |
|---|---|---|---|---|
| Crystal system | | Rhombohedral | | Rhombohedral |
| Space group | | $R3c$ | | $R3c$ |
| Z | | 6 | | 6 |
| No. of observed $F_0$ | | 610 | | 604 |
| No. of used $F_0$ | | 136 | | 129 |
| Lattice constant | | | | |
| $a$ (Å) | | 5.1529(5) | | 5.1603(7) |
| $c$ (Å) | | 13.783(7) | | 13.800(9) |
| Vol (Å$^3$) | | 316.9(4) | | 318.2(4) |
| $R_F$ | | 4.48 | | 4.41 |
| $wR_F$ | | 5.34 | | 5.31 |
| $Li^+$ | Occupancy | 1.0000 | $Li^+$ | 0.9078(6) |
| $Mg^{2+}$ | Occupancy | 0.0 | $Mg^{1.643+}$ | 0.0925(6) |
| | x | 0.0 | | 0.0 |
| | y | 0.0 | | 0.0 |
| | z | 0.3055(10) | | 0.313(12) |
| | $B_{iso}$ | 0.598(17) | | 0.595(12) |
| | $u_{11} = u_{22}$ (Å) | 0.0050(13) | | 0.0046(5) |
| | $u_{33}$ (Å) | 0.0095(8) | | 0.0103(18) |
| | $u_{12} = u_{11}/2$ (Å) | 0.0025(6) | | 0.0023(13) |
| $Ta^{5+}$ | Occupancy | 1.0000 | $Ta^{4128+}$ | 1.0000 |
| | x | 0.0 | | 0.0 |
| | y | 0.0 | | 0.0 |
| | z | 0.0 | | 0.0 |
| | $B_{iso}$ | 0.401(15) | | 0.568(21) |
| | $u_{11} = u_{22}$ (Å) | 0.0039(3) | | 0.0046(5) |
| | $u_{33}$ (Å) | 0.0049(6) | | 0.0197(7) |
| | $u_{12} = u_{11}/2$ (Å) | 0.0020(2) | | 0.0023(3) |
| $O^{20-}$ | Occupancy | 3.0000 | $O^{1729+}$ | 3.0000 |
| | x | 0.045(5) | | 0.049(3) |
| | y | 0.331(6) | | 0.337(11) |
| | z | 0.072(2) | | 0.093(5) |
| | $B_{iso}$ | 0.404(4) | | 0.556(3) |
| | $u_{11}$ (Å) | 0.0040(10) | | 0.0046(25) |
| | $u_{22}$ (Å) | 0.0039(21) | | 0.0035(33) |
| | $u_{33}$ (Å) | 0.0063(27) | | 0.0102(30) |
| | $u_{12}$ (Å) | −0.0008(20) | | −0.0007(25) |
| | $u_{13}$ (Å) | −0.0004(20) | | −0.0002(23) |
| | $u_{14}$ (Å) | −0.0002(23) | | −0.0001(33) |

## II. EXPERIMENTAL METHODS

Single crystals of stoichiometric LT and LMT with the Mg substitution of 7 mol.% were supplied from Oxide Co. The detailed crystal growth procedure and their chemical homogeneity and crystallinity have been described.[17] Angle-dispersive powder x-ray diffraction was measured with special attention paid to the precise measurement of diffraction pattern on compression and decompression to 46 GPa. The diffraction was measured using synchrotron radiation with a wavelength of 0.4262 Å, at beam lines 13-BM-D and 16-IDB (0.3115 Å and 0.3956 Å) of the Advanced Photon Source (APS), Argonne National Laboratory (ANL). A focused x-ray beam with 30 $\mu$m in diameter was aligned with the center of the sample chamber in symmetric diamond-anvil cells (DACs). The diffraction patterns were recorded with an imaging plate MAR-345 and processed with FIT2D software. The lattice parameters of the samples were determined by Rietveld profile fitting from the observed diffraction peaks. The DACs were prepared with a 200 $\mu$m culets and a 450 $\mu$m diameter tables. The sample chamber was created from a 100 $\mu$m hole drilled in a Re gasket preindented to 60 $\mu$m from the initial thickness of 200 $\mu$m. Fine powder sample and ruby chip for a pressure marker were loaded in the sample chamber. Ne is used for the pressure medium, and pressure was determined from the ruby luminescence method.[18,19]

Rietveld profile fitting analyses at various pressures were conducted from the powder diffraction patterns with increasing pressure. Since LT has a non-centric structure of $R3c$, the atomic position of Ta is fixed to (0 0 0) at a crystallographic special position. Li and oxygen have variable positional parameters of (0 0 z) and (x, y, z), respectively. Rietveld profile fitting of powder diffraction pattern was performed with the program RIETAN-2000.[20] The background intensity distribution was first adjusted for the refinement, and the lattice parameters, atomic positional coordinates, and temperature factors were treated as variable parameters. Subsequently, profile parameters (full width at half maximum, asymmetry parameters, and angular decay parameter) were varied in the refinement, and preferred orientation correction was made. Finally, a full matrix, least-squares refinement was conducted.

Single-crystal structure refinements of both LT and LMT at ambient pressure were performed using a four-circle x-ray diffractometer at synchrotron beamline BL-10 A KEK Tsukuba.[21] To determine effective charges of constituent atoms, a conventional structural refinement using single-crystal diffraction intensities was carried out by the full matrix least-squares program RADY.[22] A diamond absorption correction was applied during the analyses. Observed intensities were converted to structure factors after correction for x-ray absorption, x-ray extinction, and Lorentz and polarization effects. Structure factors $F_c(h)$ for reflections $hkl$ were calculated from the atomic position $(x_s\ y_s\ z_s)$ of $s$ atom and atomic scattering factor $f_j$ of element $j$ together with temperature factor $T_j(\boldsymbol{h})$, where $\boldsymbol{h}$ is a scanning vector. Calculated structure factors are expressed by

$$F_{cal}(\boldsymbol{h}) = K \sum_j a_j f_j(\boldsymbol{h}) \sum T_{js}(\boldsymbol{h}) \exp\{2\pi i(hx_{js} + ky_{js} + lz_{js})\}, \tag{1}$$

where $K$ is a scaling factor, $a_j$ is the site occupancy of $j$ atoms, and $f_i$ is the atomic scattering factor of $i$ ion. $T(\boldsymbol{h})$ is the thermal vibration parameter. Least-squares refinement was conducted by minimization of

$$\Delta = \sum_{\vec{h}} w(h)\{|F_{obs}(h)| - F_{cal}(h)\}^2. \tag{2}$$

Atomic coordinates, site occupancy parameters, anisotropic temperature factors, and isotropic extinction parameters were chosen as the variable parameters and results were presented in Table I. Since ferroelectric phases have a noncentric symmetry, the origin of the structure was fixed at Ta(0 0 0) in LT and LMT rhombohedral structures.

For the Raman measurements, we loaded crystals in a DAC with Ne as the pressure medium. The measurements were performed in a backscattering geometry. The measured spectra represent the sum of both polarized and depolarized components.

## III. RESULTS AND DISCUSSION

### A. Ta effective charges in (Li,Mg)TaO$_3$

The space- and time-averaged structures of the dynamical vibration of the constituent atoms of ferroelectrics can be elucidated from the electron density (ED) analysis. In the analysis, the cation site occupancy was a variable parameter in the least-square refinement, and the effective charges were evaluated from the single-crystal x-ray data. The atomic displacement due to dynamical vibration of atoms of ferroelectric materials was clarified by the refinement. Structure factor $F_c(hkl)$ in Eq. (1) was derived from the site occupancy $a_i$, atomic scattering factors $f_i$, anisotropic temperature factors $T_i(hkl)$, and isotropic extinction parameters together with atomic position ($x_i$ $y_i$ $z_i$) of atom $i$. The converged structure parameters from the refinement are presented in Tables II & III.

Here, the atomic scattering factors $f_i$ of Mg, Ta, and O are used as variable parameters in the least-square refinement in order to evaluate the effective charges of these cations. The effective charges are determined by the monopole refinement from observed $F(hkl)$ data.[23] Atomic scattering factors $f_i$ used in the conventional structure analysis are obtained from the wave function based on the Hartree-Fock approximation, and these factors are presented in Ref. 24. Note that the calculation using the isolated atom model gives an ideally spherical electron density distribution without any interaction with adjacent atoms. The $\kappa$-parameter[25,26] was applied in the atomic scattering factor, which is an indicator of the radial distributions of electron. Effective charges of atoms are obtained from the following equation in the least-squares calculation using the shell model in which the core and valence electrons are separated as follows:

$$f(s/2) = f_{j,core}(s/2) + P_{j,valence} f_{j,M-core}(\kappa_j, s/2) + f_j' + i f_j'', \quad (3)$$

where $s/2 = \sin\theta/2\lambda$ and $P_{j,valence}$ is a population of valence electron of $j$ atom. $f_j'$ and $f_j''$ are anomalous dispersion factors.

TABLE II. Rietveld analysis of LiTaO$_3$ ferroelectric $R3c$ phase.

| Press | (GPa) | 0.0001 | 5.80 | 8.82 | 13.1 | 17.6 | 21.9 | 26.6 | 28.5 |
|---|---|---|---|---|---|---|---|---|---|
| | $R_F$ | 6.09 | 8.58 | 6.98 | 4.38 | 4.34 | 2.38 | 4.17 | 8.34 |
| | $wR_F$ | 7.05 | 8.40 | 15.86 | 12.12 | 12.76 | 4.75 | 6.84 | 12.54 |
| | A(Å) | 5.1532(5) | 5.0475(5) | 5.0095(5) | 4.9722(5) | 4.9307(5) | 4.9012(2) | 4.8649(2) | 4.8504(2) |
| | c(Å) | 13.784(9) | 13.587(9) | 13.522(9) | 13.345(9) | 13.376(9) | 13.128(8) | 13.022(10) | 13.008(9) |
| | Vol (Å$^3$) | 315.9(8) | 299.7(8) | 293.8(7) | 285.7(2) | 281.6(3) | 273.1(7) | 266.9(5) | 265.0(3) |
| Li | occupancy | 0.3333 | | | | | | | |
| | x | 0.0 | 0.0 | 0.0 | 0.0 | 0.0 | 0.0 | 0.0 | 0.0 |
| | y | 0.0 | 0.0 | 0.0 | 0.0 | 0.0 | 0.0 | 0.0 | 0.0 |
| | z | 0.312(2) | 0.334(8) | 0.332 | 0.332(9) | 0.328(3) | 0.320(4) | 0.336(6) | 0.326(11) |
| | B$_{iso}$ | 1.49(3) | 0.91(8) | 1.33(4) | 1.12(8) | 1.03(8) | 1.04(8) | 0.46(21) | 1.05(16) |
| Ta | Occupancy | 0.3333 | | | | | | | |
| | x | 0.0 | 0.0 | 0.0 | 0.0 | 0.0 | 0.0 | 0.0 | 0.0 |
| | y | 0.0 | 0.0 | 0.0 | 0.0 | 0.0 | 0.0 | 0.0 | 0.0 |
| | z | 0.0 | 0.0 | 0.0 | 0.0 | 0.0 | 0.0 | 0.0 | 0.0 |
| | B$_{iso}$ | 0.15(4) | 0.70(8) | 0.58(6) | 0.77(6) | 0.40(2) | 0.76(2) | 0.79(2) | 0.59(21) |
| O | Occupancy | 1.0000 | | | | | | | |
| | x | 0.0342(9) | 0.022(4) | 0.009(6) | 0.007(2) | 0.009(14) | 0.010(8) | 0.007(10) | 0.003(13) |
| | y | 0.3325(12) | 0.335(9) | 0.324(7) | 0.324(5) | 0.333(5) | 0.328(7) | 0.326(12) | 0.329(13) |
| | z | 0.0870(2) | 0.084(5) | 0.078(7) | 0.074(4) | 0.075(3) | 0.080(4) | 0.096(14) | 0.071(13) |
| | B$_{iso}$ | 0.59(6) | 1.80(7) | 1.71(9) | 1.66(5) | 1.49(2) | 1.99(3) | 1.21(19) | 2.08(12) |
| d(Li-O) x3(Å) | | 2.0510(5) | 1.981(9) | 1.9874(7) | 1.945(9) | 1.945(8) | 1.950(6) | 1.927(8) | 1.914(13) |
| d(Li-O) x3(Å) | | 2.203(5) | 2.118(9) | 2.102(7) | 2.105(9) | 2.045(8) | 2.034(6) | 2.028(9) | 2.004(13) |
| Ratio | | 1.074 | 1.0691 | 1.0576 | 1.0822 | 1.0514 | 1.0430 | 1.0524 | 1.0470 |
| av (Å) | | 2.1357(5) | 2.049(9) | 2.044(7) | 2.025(9) | 1.995(8) | 1.992(6) | 1.978(9) | 1.959(13) |
| d(Ta-O) x3(Å) | | 1.9763(7) | 1.976(8) | 1.917(9) | 1.875(8) | 1.905(8) | 1.900(9) | 1.866(8) | 1.838(12) |
| d(Ta-O) x3(Å) | | 2.0287(7) | 1.997(8) | 2.058(8) | 2.074(8) | 2.033(8) | 1.993(8) | 2.006(8) | 2.043(12) |
| Ratio | | 1.0265 | 1.0106 | 1.0736 | 1.1061 | 1.0672 | 1.0437 | 1.0750 | 1.1153 |
| av (Å) | | 2.0025(7) | 1.986(8) | 1.987(9) | 1.975(8) | 1.969(8) | 1.941(8) | 1.936(8) | 1.940(12) |
| Vol(LiO$_6$)(Å$^3$) | | 12.371 | 11.423 | 11.355 | 11.005 | 10.584 | 10.438 | 10.217 | 9.991 |
| Vol(TaO$_6$)(Å$^3$) | | 10.699 | 10.443 | 10.456 | 10.225 | 10.152 | 9.745 | 9.579 | 9.666 |
| d(Li-O)/do | | 1.000 | 0.9594 | 0.9571 | 0.9482 | 0.9341 | 0.9327 | 0.9262 | 0.9173 |
| d(Ta-O)/do | | 1.000 | 0.9917 | 0.9922 | 0.9862 | 0.9833 | 0.9693 | 0.9668 | 0.9688 |

Detailed discussion of the derivation of the core $f_{core}$ and $f_{valence}$ have been described previously.[27] Under ambient conditions, $P_{j,valence}$ and $\kappa$-parameter are observed from the structure refinement. $P_{Ta,valence}$, $P_{Mg,valence}$, $O_{a,valence}$, $\kappa_{Ta}$, $\kappa_{Mg}$, and $\kappa_O$ of Ta and Mg are variable parameters in the calculation. The population parameter ($P$) of the valence electrons in Eq. (3) defines the effective charge. The $\kappa$-parameters and valence electrons are presented in Table IV. In order to estimate the electron density deformation by the $\kappa$-parameter, the residual factor $\Sigma(|F_{obs}|\text{-}|F_{cal}|)^2$ was minimized with the $\kappa$-parameter. The population parameter was optimized together with the $\kappa$-parameter. In the refinement, the charges of all ions are constrained to be neutral in the bulk crystal. The $\kappa$-parameters for cations in LMT are $\kappa(\text{Li}) = 1.04$, $\kappa(\text{Mg}) = 1.06$, and $\kappa(\text{Ta}) = 0.91$, in the case where the total number of valance electrons is constraint. Those in LT are $\kappa(\text{Li}) = 1.07$ and $\kappa(\text{Ta}) = 0.95$. The electron distributions on their M-O bonds are more localized, when more ionic with increase in the atomic number. A more bonding electron distribution in the covalent-bonded structure indicates a smaller $\kappa$-parameter. (A cation with $\kappa = 1.0$ has the same atomic scattering of $\sin\theta/\lambda$ with a formal charge as the Hartree-Fock calculation.) Granting that the effective charge $q$ does not change over the measured pressure range in spite of larger electron localization at higher pressure, the static dipole moment can be obtained using the observed $q$ and $\Delta r_i$

TABLE III. Rietveld analysis of the high-pressure $LiTaO_3$ perovskite phase.[a]

| Pressure | (GPa) | 32.0 | 35.3 | 38.7 | 42.3 | 46.2 |
|---|---|---|---|---|---|---|
| | $R_F$ | 2.52 | 0.92 | 1.40 | 1.99 | 1.45 |
| | $wR_F$ | 7.00 | 2.98 | 4.64 | 4.36 | 14.36 |
| | a (Å) | 5.0600(9) | 5.0585(9) | 5.0534(9) | 5.0535(9) | 5.038(6) |
| | b (Å) | 6.6244(9) | 6.5835(9) | 6.5539(9) | 6.5277(9) | 6.486(9) |
| | c (Å) | 4.5544(9) | 4.5516(9) | 4.4884(9) | 4.4576(9) | 4.447(7) |
| | Vol (Å$^3$) | 152.6(9) | 150.4(9) | 148.7(9) | 147.0(9) | 145.6(9) |
| Li | Occupancy | 1.0000 | | | | |
| | x | 0.0 | 0.0 | 0.0 | 0.0 | 0.0 |
| | y | 0.0 | 0.0 | 0.0 | 0.0 | 0.0 |
| | z | 0.5 | 0.5 | 0.5 | 0.5 | 0.5 |
| | $B_{iso}$ | 5.96(3) | 0.96(3) | 1.96(3) | 0.96(3) | 1.14(3) |
| Ta | Occupancy | 1.0000 | | | | |
| | x | 0.102(9) | 0.102(9) | 0.100(9) | 0.115(9) | 0.105(9) |
| | y | 0.25 | 0.25 | 0.25 | 0.25 | 0.25 |
| | z | 0.9752(6) | 0.968(7) | 0.974(7) | 0.997(7) | 0.972(7) |
| | $B_{iso}$ | 2.92(4) | 0.77(4) | 0.41(5) | 0.77(5) | 0.54(5) |
| O1 | Occupancy | 1.0000 | | | | |
| | x | 0.473(6) | 0.311(6) | 0.466(6) | 0.469(5) | 0.476(6) |
| | y | 0.25 | 0.25 | 0.25 | 0.25 | 0.25 |
| | z | 0.030(6) | 0.032(6) | 0.034(5) | 0.097(5) | 0.096(5) |
| | $B_{iso}$ | 3.10(6) | 1.41(6) | 1.02(6) | 1.41(6) | 0.86(6) |
| O2 | Occupancy | 2.0000 | | | | |
| | x | 0.337(7) | 0.419(7) | 0.679(7) | 0.336(7) | 0.331(7) |
| | y | 0.025(5) | 0.026(7) | 0.315(7) | 0.008(7) | 0.08(7) |
| | z | 0.668(4) | 0.719(7) | 0.685(9) | 0.667(5) | 0.655(9) |
| | $B_{iso}$ | 5.05(6) | 1.06(6) | 1.07(7) | 3.05(7) | 1.12(7) |
| d(Li-O1) x3(Å) | | 1.712(3) | 1.701(4) | 1.693(4) | 1.696(6) | 1.681(6) |
| d(Li-O2) x3(Å) | | 1.861(2) | 1.850(3) | 1.855(4) | 1.836(6) | 1.825(6) |
| d(Li-O2) x3(Å) | | 1.769(2) | 1.757(3) | 1.748(4) | 1.741(6) | 1.714(6) |
| av (Å) | | 1.781(3) | 1.772(3) | 1.765(4) | 1.758(6) | 1.738(6) |
| d(Ta-O1) (Å) | | 1.948(2) | 1.946(3) | 1.944(4) | 1.865(8) | 1.893(5) |
| d(Ta-O1) (Å) | | 2.085(2) | 2.069(3) | 2.057(4) | 2.033(8) | 2.027(5) |
| d(Ta-O2) x2(Å) | | 2.396(2) | 2.383(3) | 2.373(3) | 2.398(7) | 2.357(5) |
| d(Ta-O1) x2(Å) | | 2.095(3) | 2.086(3) | 2.099(3) | 2.199(7) | 2.215(5) |
| d(Ta-O2) x2(Å) | | 2.023(3) | 2.086(3) | 2.003(3) | 1.886(7) | 1.895(5) |
| av (Å) | | 2.133(3) | 2.122(3) | 2.113(3) | 2.108(7) | 2.106(6) |
| Tolerance factor | | 0.847 | 0.847 | 0.855 | 0.848 | 0.857 |
| Vol(LiO6) (Å$^3$) | | 7.432 | 7.321 | 7.238 | 7.004 | 6.802 |
| d(Li-O)/do | | 1.0000 | 0.9949 | 0.9910 | 0.9871 | 0.9759 |
| d(Ta-O)/do | | 1.0000 | 0.9948 | 0.9906 | 0.9883 | 0.9873 |

[a] $R_F$ and $wR_F$ are expressed the following equations: $R_F\left[\frac{\Sigma_k|F_{k\,obs}|F_{k\,cal}|}{\Sigma_k F_{k\,obs}}\right], wR_p = \left[\frac{\Sigma_i w_i|y_i - f_i(x)|}{\Sigma_i w_i y_i}\right]^{1/2}$, where $F$ indicate the structure factor, $y_i$ is the observed diffraction intensity at the $i$-th position in $2\theta$, and $f$(x) is the calculated intensity. A variable $w$ is a weight for each data points.

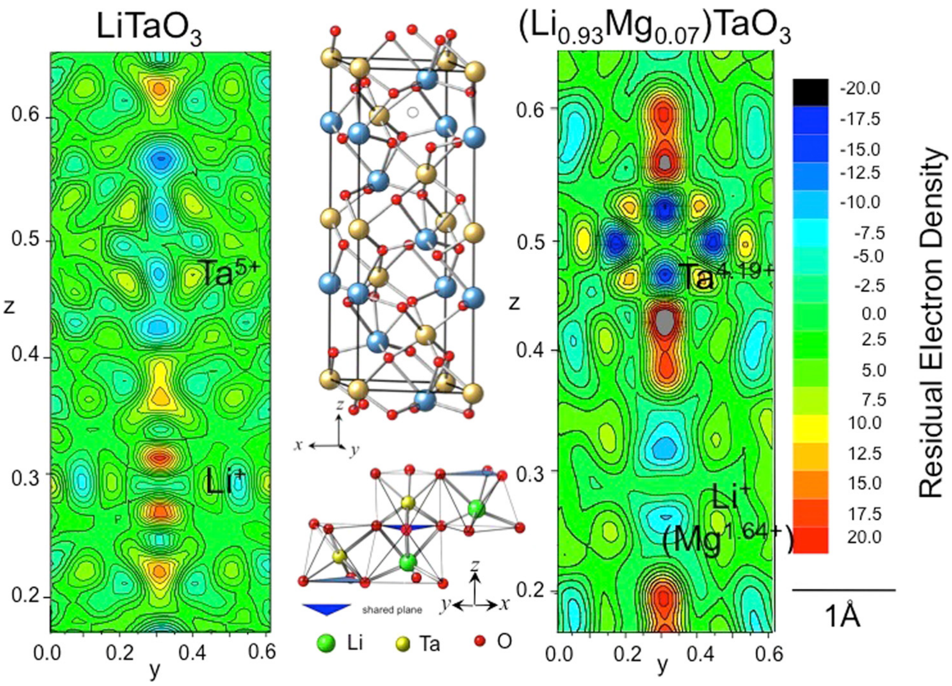

FIG. 1. Difference Fourier maps of the section of z = 0.0 and z = 0.3 on the projection on to (001) of LiTaO$_3$ (LT) and (Li,Mg)TaO$_3$ (LMT) rhombohedral *R*3*c* phase at ambient conditions. The residual electron density around Ta (0 0 0) and Li (0 0 0.300) do not show the noticeable deformation in the directions of the *a* and *b* axes.

in the direction of the *c* axis with increasing pressure; the classical definition moment $\Sigma q_i \Delta r_i$ is lowered in the rhombohedral phase.

The inverse Fourier of *F*(***h***) gives electron density *r*(xyz) at position (xyz) in the real space by $\rho(xyz) = \frac{1}{V}\sum_h \sum_k \sum_l F(\boldsymbol{h}) \exp\{-2\pi i(hx + ky + lz)\}$. Difference Fourier (DF) synthesis by $|F_{obs}(\boldsymbol{h})|$ - $|F_{cal}(\boldsymbol{h})|$ provides the comprehension of the deformation of electron distribution and bond character from the residual ED. Non-spherical deformation ED can be expressed by the difference ED $\Delta\rho$(xyz)

$$\Delta\rho(xyz) = \frac{1}{V}\sum_h \sum_k \sum_l \{|F_{obs}(\boldsymbol{h})| - |F_{cal}(\boldsymbol{h})|\} \exp\{-2\pi i(hx + ky + lz)\}. \quad (4)$$

The polarization and dipole moment are related to dielectric susceptibility, elastic properties, and strain and stress tensors. The definite orientation and anisotropy in the dynamical phenomena arise from the elasticity of the crystal. A harmonic oscillation model is a good approximation in most cases using the ellipsoidal vibration represented by ellipsoidal second-rank anisotropic thermal parameters $u_{ij}$ (Table II).

The calculated structure factors $F_{\mathrm{calc}}(hkl)$ for the difference Fourier $|F_{obs}(hkl)|$ - $|F_{cal}(hkl)|$ of LT and LMT at ambient conditions are derived in comparison with the fully ionized model: (i.e., Li$^+$, Mg$^{2+}$, and Ta$^{5+}$). DF maps of LT and LMT are the projections on (010) plane at the section of y = 0.0 in the region from $-2$ e/Å$^3$ to 2 e/Å$^3$ (Fig. 1). The maps show the residual electron density distribution indicating the polarization in the direction of [001]. However, the maps projected on (001) in the section z = 0.0 and z = 0.3 indicate no polar character in the direction of [100] and [010] (Fig. 2). The DF map of LMT compared with LT shows a more distinct ED distribution in the direction of the *c* axis around the Ta position than that of Li atomic position. The plausible fully ionized Ta$^{5+}$ induces the residual electron density from the excess electron,

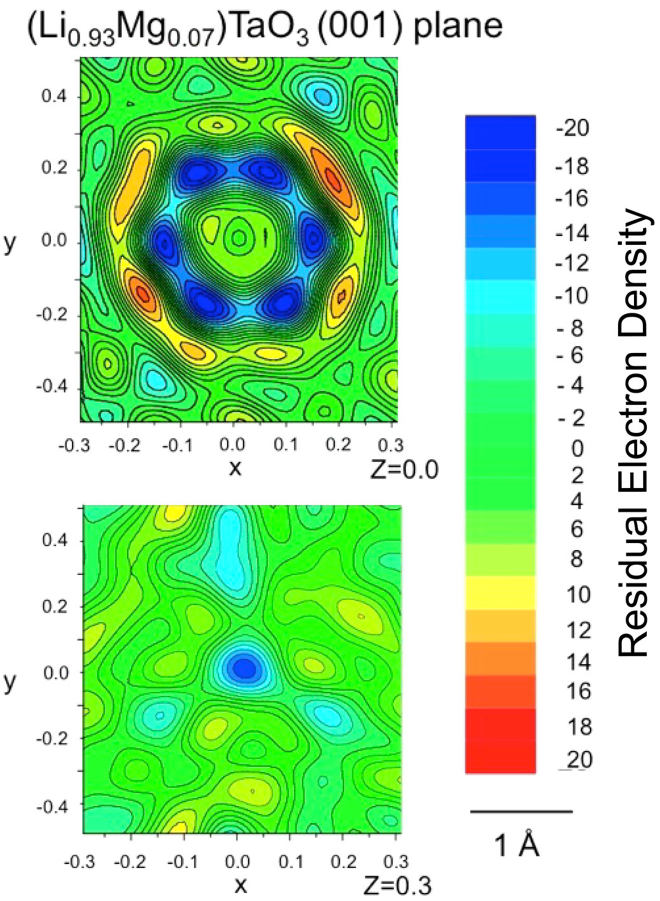

FIG. 2. Difference Fourier map of the rhombohedral (*R*3*c*) (Li,Mg)TaO$_3$ phase at ambient conditions on the projection of (010) plane at y. 0.0. The residual electron density distribution is shown in the direction of the c axis. The interval of electron contour is 0.2 e/Å$^3$ in the region from 2 e/Å$^3$ to 2 e/Å$^3$. The lower figure shows that Li and Ta octahedra are alternately located in the same layer. Li and Ta octahedra share the plane perpendicular to the c axis, while these atoms are connected with shared edges in the direction parallel to the c axis.

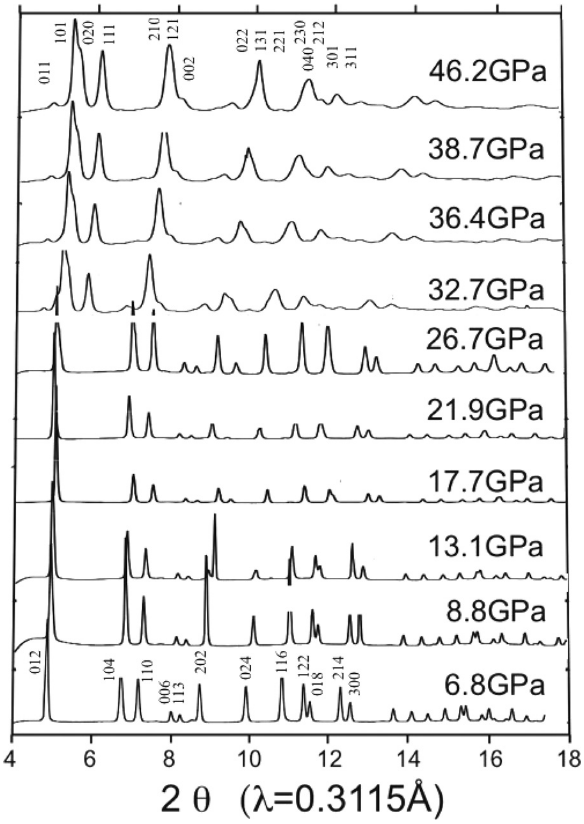

FIG. 3. Powder x-ray diffraction pattern of $LiTaO_3$ with increasing pressure.

because Ta is less ionized to $Ta^{4.13+}$ with more electrons. This is consistent with the result of the structure refinement, which is indicated by the highest reliable factor with the cation distribution of stoichiometric model. The cation distribution of $(Li_{0.9075}Mg_{0.0925})Ta_{1.0}O_3$ is confirmed by the calculation of LMT. In consideration of both site occupancy and effective charge analysis, $Ta^{5+}$ is reduced to $Ta^{4.128+}$ and $Mg^{2+}$ is changed to $Mg^{1.643+}$. The present structure refinement of LMT thus gives $(Li^{+}_{0.908}Mg^{1.643+}_{0.092})Ta^{4.128+}_{1.0}\ O^{1.729-}_{3}$. The observed occupancy is somewhat larger than the 7 mol.% substitution of Mg in the LMT sample studied.

The deformation of electron density distributions is evident by DF map on the plane (010) (Fig. 1). Residual electron density with a height of 0.7 e/A$^3$ is found in the Ta-O bond in the *c* axis direction and is found to be 0.43 Å from the metal position. The non-spherical residual electron density around the cation sites is probably induced from $d$-$p$-$\pi$ bonding involving the $5d_{xz}$- and $5d_{yz}$-electrons of Ta and $2p_x$- and $2p_y$-electrons of oxygen, which is located at 1.117 Å with 0.2 e/Å$^3$ from the Ta position. The observed $\kappa$-parameter and effective charge of the converged atomic scattering $f_i$, and residual electron found in the DF map of LT and LMT are presented in Table IV. The observed deformation of electron density of LMT indicates that it has a larger ferroelectric efficiency than LT. Ferroelectric character of LT is mainly caused the ED deformation of the Li atoms. The ED around Ta atom shows neither a noticeable deformation nor obvious residual electron density and is almost spherical.

### B. Rhombohedral (Li,Mg)$TaO_3$

The structure of Mg-doped sample LMT is an important subject to understand from the standpoint of the ferroelectricity of the $LiNbO_3$-type rhombohedral structured materials. A structural comparison between LT and LMT is therefore useful for clarifying the effect of Mg-doping on nonlinear optical and electric conductivity properties. The effects of substitution and defects in LMT rhombohedral ferroelectrics have been investigated.[15] $Mg^{2+}$ occupies the vacant sites of Li and Ta, and the $T_C$ increases with increasing Mg substitution. Stoichiometric and non-stoichiometric models with fully ionized and formal charges, $Li^+$, $Ta^{5+}$, and $Mg^{2+}$, have been proposed:

- $[Li_{1-5x-3y}\ Mg_{4y/3}\ Ta_x\ V_{4x+5y/3}][Ta_{1-8y/3}Mg_{8y/3}]\ O_3$ for stoichiometric,
- $[Li_{1-5x-3y}\ Mg_{4y/3}\ Ta_{x/4}\ V_{19x/4+5y/3}][Ta_{1+3x/4-5y/3}Mg_{8y/3}\ V_{-3x/4}]O_3$ for non-stoichiometric with $x < 0$,
- $[Li_{1-5x-3y}\ Mg_{5y/3}\ Ta_{x/5}\ V_{24x/4+4y/3}][Ta_{1+4x/5-7y/3}Mg_{7y/3}\ V_{-4x/5}]O_3$ for non-stoichiometric with $x > 0$,

where V denotes the vacancy.

If we apply effective charges instead of the formal charges, the stoichiometry can be preserved without vacancies in order to maintain neutrality of the bulk crystal. We test the cation distribution using the structure refinement. Site occupancy $a_i$ in the least-square calculation in Eq. (1) is a variable parameter. Generally, Mg in these oxides is preferentially located in the octahedral site (owing to its ion radius of 0.72 Å).[28] Li and Mg are placed in the octahedral B site in the $A^{VIII}B^{VI}O_3$ orthorhombic perovskite. The following cation distribution model is obtained from the least-square calculation:

$$(Li^{+}_{1-t}Mg^{2+}_{t})^{VI}(Ta^{5+(1-t)})^{VIII}O_3.$$

The converged site occupancies in the least-square calculation are presented in Table IV.

### C. Rhombohedral $LiTaO_3$

Li and Ta octahedra in LT are alternately located in the same layer and share the plane perpendicular to the *c* axis, while they are connected with shared edges in the direction parallel to the *c* axis. $LiO_6$ and $TaO_6$ octahedra have antiparallel di-trigonal pyramids. Powder diffraction patterns with increasing pressure up to 46.2 GPa are presented in Fig. 3, those with decreasing pressure in Fig. 4. From ambient pressure to 28.5 GPa, the rhombohedral LT phase with *R*3*c* was found to and persist other phases were detected. Above that pressure, a structured transition to a high-pressure phase was found. The phase was found to be the orthorhombic perovskite structure (*Pnma*).[16] For comparison, in Fig. 5, we show x-ray diffraction patterns at selected pressures for both LT and LMT. The spectra before and after the transitions are also shown in Fig. 5.

The significant difference in x-ray scattering power of Li (atomic number 3) and Ta (atomic number 73) complicates the diffraction measurements for LT. The powder diffraction intensity is strongly affected by the Ta atomic position. The atomic positions of $LiNbO_3$-type structure (*R*3*c*, Z = 6) were taken for the initial model of the least

TABLE IV. Occupancy, effective charge, and $\kappa$-parameter of the $R3c$ ferroelectric phase.

| | $LiTaO_3$ | | $Li_{0.93}M_{0.07}TaO_3$ | |
|---|---|---|---|---|
| Occupancy | Li | 1.0 | LI | 0.9075 |
| | | | Mg | 0.0925 |
| | Ta | 1.0 | Ta | 1.0 |
| | O | 3.0 | O | 3.0 |
| $\kappa$-parameter | $\kappa(Li)$ | 1.07 | $\kappa(Li)$ | 1.04 |
| | | | $\kappa(Mg)$ | 1.06 |
| | $\kappa(Ta)$ | 0.95 | $\kappa(Ta)$ | 0.91 |
| Effective charge | Li | $1.0^+$(fix) | Li | $1.0^+$ |
| | | | Mg | $1.643^+$ |
| | Ta | $5.0^+$(fix) | Ta | $4.129^+$ |
| | O | $2.0^1$(fix) | O | $1.732^1$ |

squares refinement of LT and LMT. The fitting results indicate a reliable profile analysis by the reliability factors of $R_F$ and $wR_F$ (Table II). Lattice parameters of LT with increasing pressure were obtained by the Rietveld profile fitting. Bond distances of Li-O and Ta-O were calculated from the observed lattice parameters and atomic positions (Table II).

The displacements of these cations from the center of the octahedra cause the extremely large difference in two bond distances in both Li and Ta octahedra, an effect that gives rise to the ferroelectric behavior. The difference in Li-O bonds decreases with increasing pressure, as indicated by the bond ratios. On the other hand, in Ta-O, the difference in the bond ratios is enhanced. These changes with pressure increase the deformation of LT and give rise to the structural transition to the orthorhombic perovskite structure.

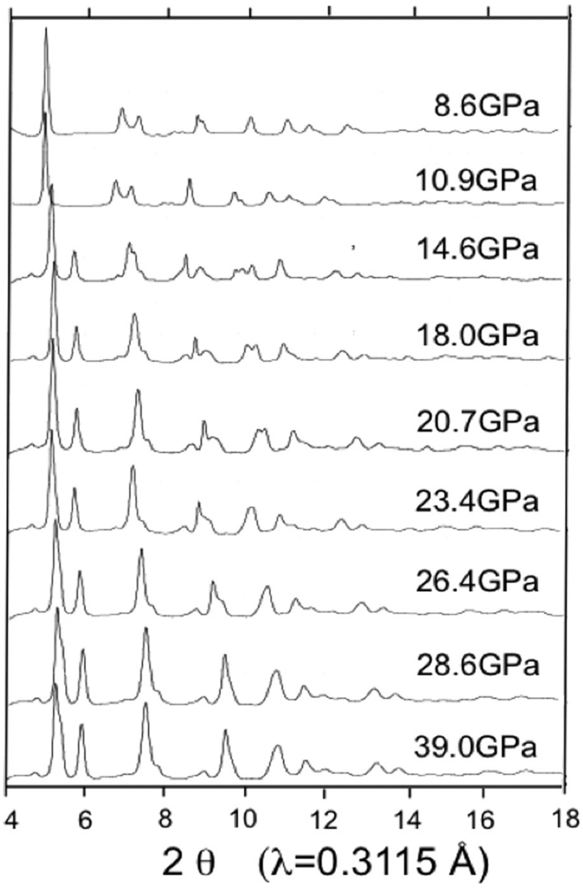

FIG. 4. Powder x-ray diffraction pattern of $LiTaO_3$ with decreasing pressure.

The octahedral volumes of both $LiO_6$ and $TaO_6$ and their ratio $V/V_o$ are also presented in Table II. The change of the unit cell volume is shown Fig. 6. The compression curve is continuous up to 28.5 GPa. The compression shows a large drop at 30 GPa and a different behavior above the pressure. On decompression, the high-pressure phase compression back transforms to the initial rhombohedral phase at 11 GPa, indicating the transition is reversible with hysteresis. Thus, the high-pressure phase is not quenchable.

Bond distance changes clarify the compression of Li and Ta octahedra with pressure. The mean bond distance is larger for Li-O than for Ta-O (Fig. 7). Ionic radii of these cations reflect the difference in the both distances. The ion radii of the formally charged ions with 6-fold coordination are $r(Li^+) = 0.76$ Å and $r(Ta^{5+}) = 0.64$ Å (Ref. 28) at ambient conditions. The $LiO_6$ octahedral volume is more compressive than that of the $TiO_6$. Since fully ionic $Li^+$ has only 2 electrons but $Ta^{5+}$ has 68 electrons (without any valence electron according to their electron configurations), the compressibility of the site volume is reasonable for the number of core electrons. Both bond length of Li-O and octahedral volumes $LiO_6$ are compressed and approach those of Ta-O and $TaO_6$ at 28.5 GPa.

### D. Orthorhombic $LiTaO_3$ above 30 GPa

Above 30 GPa, the ferroelectric rhombohedral phase of LT transforms to a high-pressure phase of paraelectric orthorhombic perovskite *Pnma* structure. This structural transition has been reported at 33 GPa.[13] In the conventional orthorhombic $ABO_3$ perovskite, a large cation occupies the 8-fold coordinated A site and a small cation is located in the octahedral B site. The present refinement was used to test the cation distribution in the sites of A(x y 1/4) and B(0 1/2 0) in the orthorhombic perovskite structure. The test proves that Li is located in the crystallographical special-position of Li(0 1/2 0), which is the smaller B site and Ta is in the variable position of Ta($x$ $y$ 1/4) referring to the reliable factor $R_F$ and $wR_F$. Oxygen has two positions, O1 ($x$ $y$ 1/4) and O2($x$ $y$ $z$). The observed orthorhombic structure is shown in Fig. 8.

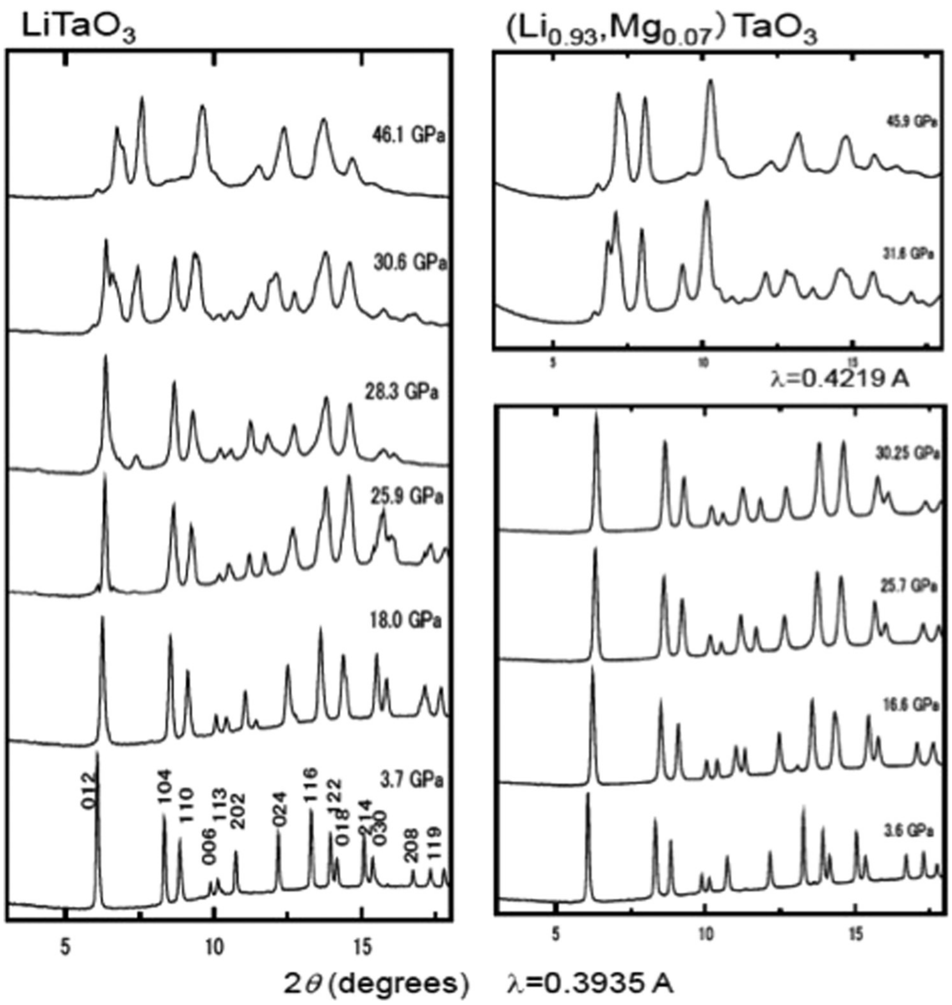

FIG. 5. Powder x-ray diffraction patterns of $LiTaO_3$ and $(Li,Mg)TaO_3$ at selected pressures for comparison.

The observed radii differ from those determined at ambient pressure. Bond distances of Li-O and Ta-O with increasing pressure are shown in the table. Li-O distance in the rhombohedral structure contracts from 2.4 Å at ambient conditions to 1.96 Å at 28.5 GPa. The $LiO_6$ octahedra become more regular as indicated by bond ratio (Table II). The average octahedral Li-O distance of the perovskite structure is compressed to 1.78 Å at 32 GPa (Table III). The Ta site changes its coordination from 6-fold in *R*3*c* to 8-fold in *Pnma*. The average Ta-O bond distance in the perovskite

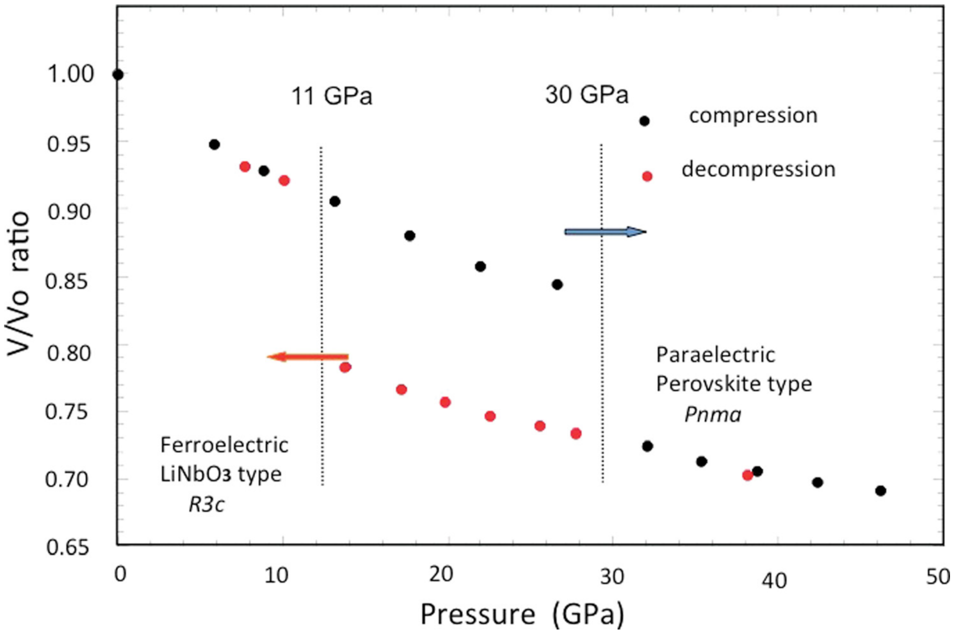

FIG. 6. Relative unit cell volumes ($V/V_0$) of both ferroelectric rhombohedral and paraelectric orthorhombic phases as a function of pressure.

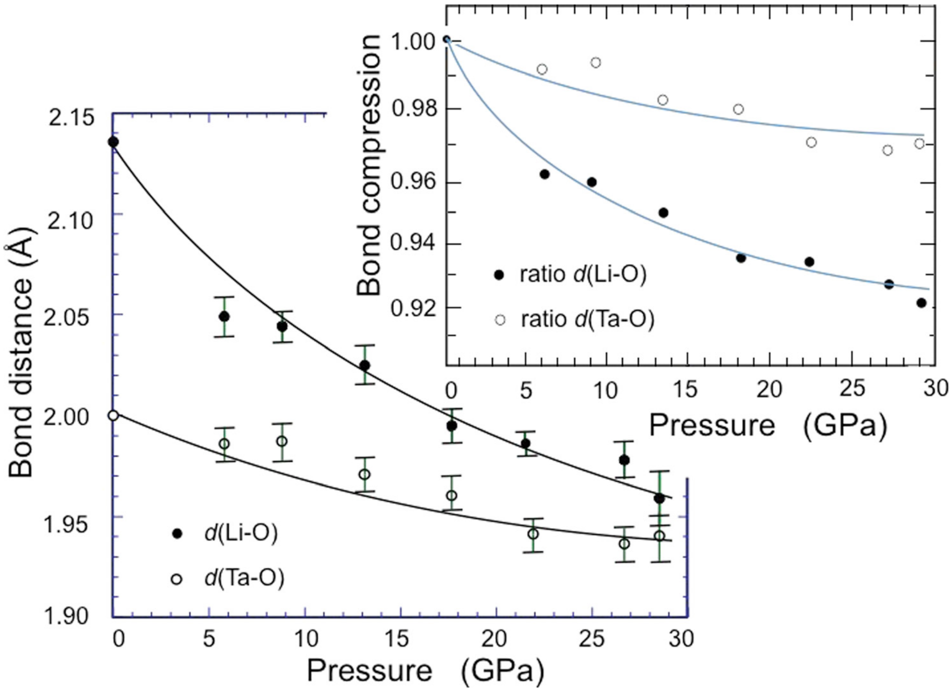

FIG. 7. Pressure dependencies of Li-O and Ta-O bond distances in the rhombohedral phase of $LiTaO_3$ up to 30 GPa.

structure is much larger than that in the rhombohedral structure because of the different coordination. On further compression up to 46.2 GPa, Li-O bond is more compressed than Ta-O bond. However, the tolerance factor $t$: $t = (r_A + r_O)/\sqrt{2}(r_B + r_O) \cong d_{(Ta\text{-}O)}/\sqrt{2}d_{(Li\text{-}O)}$ is $t = 0.85$ in all pressure range.

### E. Thermal factors

The asymmetric polarization and conductivity of LT have been confirmed by systematic time-temperature measurements.[29] The anisotropic atomic vibration is observed as positional disorder and thermal vibration of atoms. Our electron deformation analysis in the pressure dependence of the anisotropy in electric conductivity of ilmenite $FeTiO_3$ by the DF map[30] shows the noticeable anisotropic residual electron density. The anisotropic atomic vibration can be evaluated by the anisotropic temperature $T(hkl)$ [Eq. (1)].

The features of the ED maps on (010) and (001) projections (Figs. 2 and 3) are interpreted in two ways: one is static positional disorder (lattice average) and the other is dynamical disorder (time average) of the atomic vibration in the crystal structure. The overall temperature factor $B_{iso}$ and anisotropic temperature factors $u_{ij}$ in $T(hkl)$ are indicators of the thermal vibrations of atoms and atomic positional disorder by the following second rank anisotropic temperature factors $u_{ij}$:

$$
\begin{aligned}
T(hkl) = \exp\{&-2\pi^2(u_{11}h^2a^{*2} + u_{22}k^2b^{*2} + u_{33}l^2c^{*2} \\
&+ 2u_{12}hka^*b^*\cos\gamma^* + 2u_{13}hla^*c^*\cos\beta^* \\
&+ 2u_{23}klb^*c^*\cos\alpha*), \qquad (5)
\end{aligned}
$$

where $u_{ij}$ is a mean square displacement of the amplitude of atomic thermal motion. Since the site symmetry of Li and Ta site is $3m$ and that of O is 2 in the space group $R3c$, the following constraint in $u_{ij}$ is applied in the least-square calculation: for Li and Ta: $u_{11} = u_{22}$, $u_{33}$, $u_{12} = u_{11}/2$, $u_{11} = u_{11} = 0$, and for O: $u_{11}$, $u_{22}$, $u_{33}$, $u_{12}$, $u_{13}$, $u_{23}$.

The light atom Li has a larger $B_{iso}$ relative to the Ta in both LT and LMT and $u_{33}$ of the both atoms in LMT along the $c$ axis is much larger than $u_{11}$ ($= u_{22}$) along the $a$ and $b$ axes. The elongation of ED in the DF map (Fig. 1) is in a good agreement with $u_{ij}$ observed in the refinement. The anisotropy of thermal vibration of Ta is distinguished by the large $u_{33}$. The residual electron density induced from the excess electron along the $c$ axis in LMT indicates more electrons around the Ta site, as confirmed by the effective charge analysis. On the other hand, LT displays an obvious anisotropy of Li, which may be the evidence of the ferroelectricity of $LiTaO_3$. The refinement of the temperature factors is

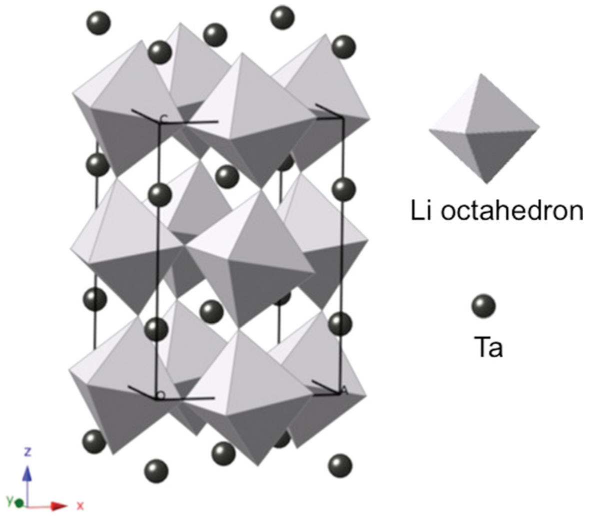

FIG. 8. High-pressure phase of $LiTaO_3$ with orthorhombic perovskite structure Pnma. Li atom is located at the octahedral site. Ta is placed in the void space and has an 8-fold coordination.

consistent with the residual electron density presented by DF map.

The isothermal bulk modulus $K_o$ and its pressure derivative $K_o'$ determined from second-order Birch-Murhagham equation of state[31] fits of the cell volumes with pressure give

LT: $K_o = 95(5)$ GPa $K_o' = 5.9(0.7)$
LMT: $K_o = 103(9)$ GPa $K_o' = 6.1(1.4)$.

The two materials show the different transition pressures: 28 GPa for LT and 33 GPa for LMT.

Xiang *et al.*[16] reported $K_o = 116$ GPa and $K_o' = 6.6$ for LT based on a Birch-Murnaghan equation of state fit. The slightly larger $K_o$ reported by Xiang *et al.*[16] may be associated with the stiffer pressure transmitting medium (silicon oil) used in those experiments.

### F. Raman scattering

Figures 9 and 10 show the results of Raman measurements for the two materials. Representative Raman spectra for LT at selected pressures are shown in Fig. 9(a), and a comparison LT and LMT at 7 GPa is shown in Fig. 9(b). The spectra of the two measurements are almost identical. In its ferroelectric phase, the point group symmetry of LT is $C_3v$. Thus, the irreducible representations of optical vibrational modes are

$$\Gamma_{opt} = 4A_1(\mathrm{Z}) + 9E(X,Y) + 5A_2, \qquad (6)$$

where $A_1$ and E are Raman, infrared, and hyper-Raman active, whereas the silent $A_2$ modes are only hyper-Raman active. Assuming each excitation to be represented by a Lorentzian function (e.g., Fig. 10(a)), we assign peaks (ambient pressure frequencies) at 215 $\mathrm{cm}^{-1}$, 231 $\mathrm{cm}^{-1}$, 326 $\mathrm{cm}^{-1}$, 609 $\mathrm{cm}^{-1}$, to $A_1$ (TO) modes and peaks at 148 $\mathrm{cm}^{-1}$, 272 $\mathrm{cm}^{-1}$, 294 $\mathrm{cm}^{-1}$, 378 $\mathrm{cm}^{-1}$, 412 $\mathrm{cm}^{-1}$, 472 $\mathrm{cm}^{-1}$, to E (TO) modes (Fig. 9(a)). We also observed three peaks from silent $A_2$ (TO) mode. We did not attempt polarization experiments because stressed diamond anvils tend to scramble the polarization of the light. Our focus is on the pressure dependencies of the more intense Raman bands.

Figure 10(b) shows the pressure dependencies of each Raman mode obtained by a multipeak fitting procedure. We found that most peaks harden on compression and several peaks show non-linear dependencies with pressure. In particular, peaks at 272 and 294 $\mathrm{cm}^{-1}$ merge together above 8 GPa; this is accompanied by the appearance of a peak at 256 $\mathrm{cm}^{-1}$ and 550 $\mathrm{cm}^{-1}$. This behavior is similar to that of $\mathrm{PbTiO_3}$ (PT) and Pb-based relaxors. For example, in $\mathrm{PbTiO_3}$, two peaks merge around 11 GPa, which correspond to the

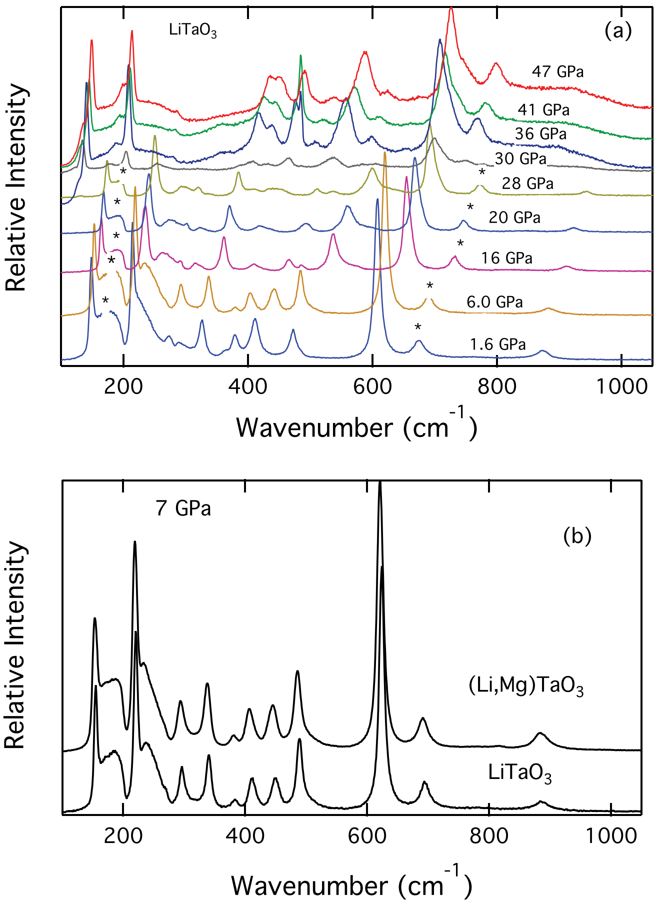

FIG. 9. (a) Representative Raman spectra of single-crystal $\mathrm{LiTaO_3}$ at selected pressures. Stars indicate second-order Raman peaks; and spectra below 20 $\mathrm{cm}^{-1}$ were filtered out using notch filter. (b) Comparison of Raman spectra between LT and LMT at 7 GPa.

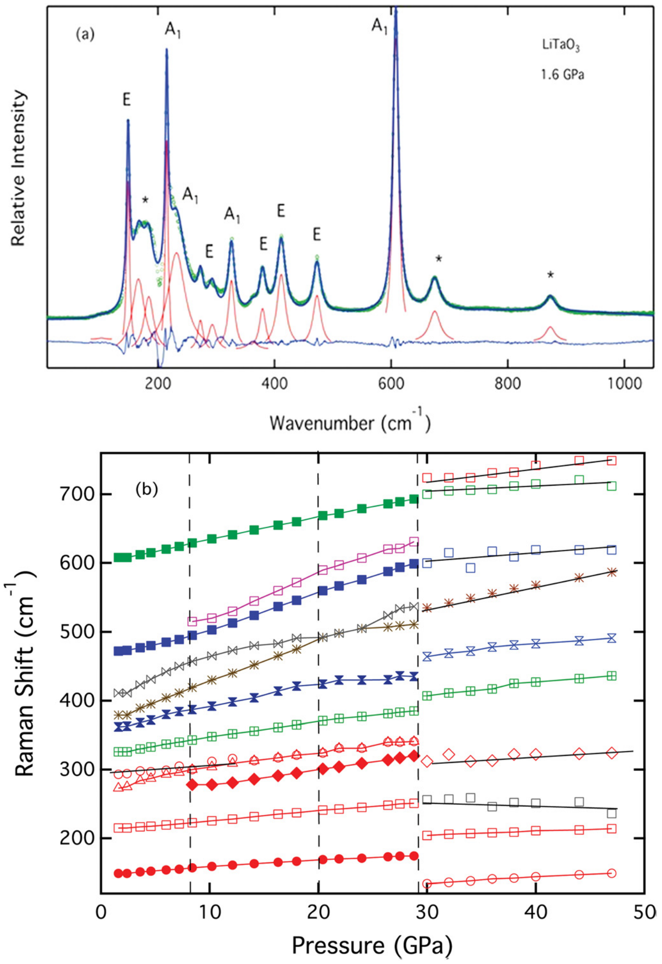

FIG. 10. (a) Example of a multipeak fit for single crystal $\mathrm{LiTaO_3}$ at 1.6 GPa. The points are experimental data and curves are fits. (b) Pressure dependencies of Raman modes up to 50 GPa. Symbols are the measured points and lines or curves are guides to the eyes.

ferroelectric to paraelectric transitions.[32] In relaxor materials, PMN-PT[33,34] or PZN-PT,[35] merging of two peaks are accompanied with the appearance of a new peak near 370 cm$^{-1}$, and transitions occur between 4 and 7 GPa. The similar behavior occurs at 8 GPa in both LT and LMT. However, it should be noted that because of the distance difference between Li-O and Ta-O bonds is approaching each other under pressure; thus, these two modes approach each other with pressure. In addition, to verify whether the pressure-induced structural transitions in LT and LMT were associated with soft optical phonon, we investigated the pressure dependence of the lowest phonon mode and shown in Fig. 11; however, we found no soft optical involved in this transition.

Other changes in Raman spectra occur around 20 GPa. Two Raman peaks between 350 and 450 cm$^{-1}$ merge above 20 GPa. At this stage, we do not know the origin for this change, but these two peaks show different pressure dependencies, the lower one shows a linear pressure dependence and increases with pressure linearly, whereas the higher frequency one shows non-linear behavior with pressure, first increasing with pressure and then becoming flat with pressure above 20 GPa. These two peaks thus crossover around 20 GPa, and because no other changes were observed up to 28 GPa, we do not associate this with a structural transition.

Additional changes in the Raman spectra occur at higher pressure. The Raman spectra show major changes above 28 GPa for LT and 33 GPa for LMT, respectively. The Raman spectra features of LT are completely different below and above 28 GPa, accompanied with the disappearance of several Raman peaks and appearance of several new Raman peaks (Fig. 9). We thus identify the second transition at 28 GPa and 33 GPa in LT and LMT, respectively. These changes in the Raman spectra are accompanied with a large volume collapse consistent with the structural transformation from the *R*3c to *Pnma* phase.

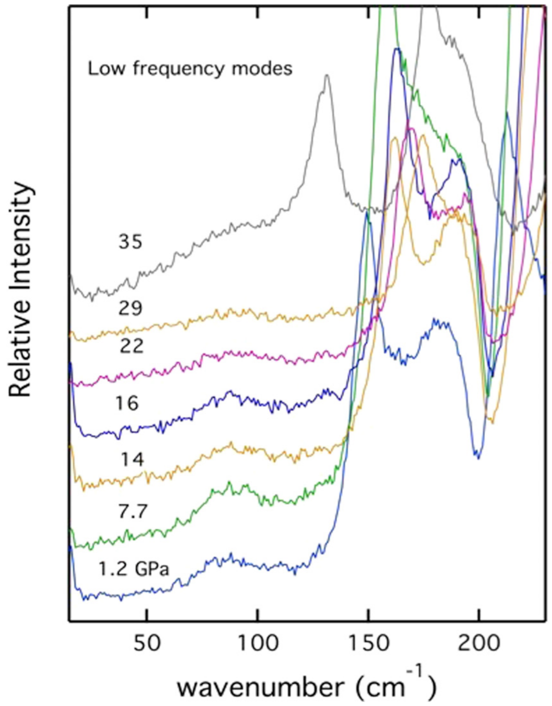

FIG. 11. Representative low-frequency Raman spectra of Mg$_{0.07}$Li$_{0.093}$TaO$_3$ at selected pressures.

A combination of Raman scattering and x-ray diffraction was further employed to investigate the behavior of LT and LMT up to 50 GPa at 300 K. The Raman spectra show drastic changes indicating of a structural transition for both LT and LMT. Our x-ray diffraction results reveal that structural transition is first-order, from a rhombohedral *R*3c to orthorhombic *P*nma. We also find that Mg doping specimen has a minimal effect on the phase transition.

## IV. CONCLUSIONS

Both x-ray powder diffraction and Raman scattering experiments indicate LF ferroelectric rhombohedral phase of *R*3*c* with Z = 6 transforms to paraelectric orthorhombic perovskite structure of *Pnma* with Z = 4 at 30 GPa. The bond length of Li-O is enormously compressed to the close values of Ta-O with increasing pressure. In the high-pressure perovskite, Li is located in the smaller octahedral site than Ta site with the 8-fold coordination. The Mg-doped sample (LMT) enhances the property of nonlinear optics and efficiency of ferroelectricity. Difference Fourier of LT and LMT shows the noticeable residual electron density distribution, indicating the polarization in the direction of the *c* axis and a more distinct electron density distribution around the Ta position in LT in comparison with that of LT.

The deformation of ED distributions discloses that ferroelectric property of LT is mainly caused by the deformation of the light element of Li. On the other hand, in the Mg-doped LMT with the high efficiency of ferroelectricity, ED around Ta atom shows a noticeable deformation and obvious residual electron density and confirms the Mg replacement at the Li site.

The effective charges analysis of LMT by the monopole refinement from observed *F(hkl)* data shows Ta$^{4.128+}$, Mg$^{1.643+}$, and O$^{1.729}$, indicating a stoichiometric (Li$^{+}_{0.908}$ Mg$^{1.643+}_{0.092}$)Ta$^{4.128+}_{1.0}$O$^{1.729-}_{3}$. The present result is strikingly different from the previous discussion of the enhancement of the ferroelectric property of LMT based on the fully ionized cations' model of the nonstoichiometric structure with vacant sites. LMT is composed of not fully ionized and the present difference Fourier is consistent with the view that the non-spherical residual electron density around the cation sites is induced from $d$-$p$-$\pi$ bonding between 5$d_{xz}$- and 5$d_{yz}$-orbitals of Ta and 2$p_x$- and 2$p_y$-orbitals of oxygen. Anisotropic temperature factors *u*ij of *T(hkl)* in the single crystal structure refinement elucidates the space- and time-averaged structures of the dynamical vibration of atoms. The refinement of temperature factor is consistent with the cation distribution of deformation of electron cloud along the *c* axis in the rhombohedral ferroelectric phase.

We assigned all peaks observed at ambient pressure to A$_1$ (TO) modes and to E (TO) modes. The pressure dependencies of each Roman mode were obtained by a multipeak fitting procedure. Raman spectra show drastic change at 28 GPa for LT and 33 GPa for LMT due to the structural transition from *R*3*c* to *Pmna* and consistent with the x-ray diffraction results. Raman scattering of LT and LMT reveal the anomalous changes in several Raman peaks. The two Raman peaks centered at 250 $\mathrm{cm}^{-1}$ and 350 $\mathrm{cm}^{-1}$ at ambient pressure merge together above 8 GPa due to the diminishing distance difference between Li-O and Ta-O bonds with pressure in both LT and LMT.

## ACKNOWLEDGMENTS

This work was partially sponsored by the Carnegie/DOE Alliance Center (CDAC, DE-NA-0002006); DOE-BES (DE-FG02-06ER46280); and EFree, an Energy Frontier Research Center funded by the U.S. Department of Energy (DE-SC-0001057; salary support for M. A.). H.K.M. was funded by the U.S. National Science Foundation Grant Nos. EAR-1345112 and EAR-1447438. Work performed at HPCAT (Sector 16), Advanced Photon Source (APS), Argonne National Laboratory was supported by DOE-NNSA under Award No. DE-NA0001974 and DOE-BES under Award No. DE-FG02-99ER45775, with partial instrumentation funding by NSF. APS is supported by DOE-BES, under Contract No. DEAC02-06CH11357. Experiments at KEK were supported by Grant No. 2012G195 for single crystal diffraction at BL-10A of the Photon Factory, Tsukuba, Japan.

[1] S. C. Abraham and J. L. Bemstein, J. Phys. Chem. Solids **28**, 1685–1692 (1967).
[2] R. Hsu, E. N. Maslen, D. Boulay, and N. Ishizawa, Acta Cryst. B **53**, 420–428 (1997).
[3] K. Nassau, H. J. Levenstein, and G. M. Loiacono, J. Phys. Chem. Solids **27**, 983–988 (1966).
[4] S. C. Abraham, W. C. Hamilton, and A. Sueira, J. Phys. Chem. Solids **28**, 1693–1698 (1967).
[5] H. Boyson and F. Altorfer, Acta Cryst. B **50**, 405–414 (1994).
[6] E. J. Samuelsen and A. P. Grande, Z. Phys. B: Condens. Matter **24**, 207–210 (1976).
[7] A. M. Glass, Phys. Rev. **172**, 564–571 (1968).
[8] J. Kushibiki, Y. Ohashi, and N. Mishima, IEEE Trans. Ultrason. Ferroelectr. Freq. Control **50**, 544–552 (2003).
[9] K. Maaider, A. Jennane, N. Masaif, and A. Khali, M. J. Condens. Matter **12**, 149–154 (2010).
[10] I. Tomeno and S. Matsumura, Phys. Rev. B **38**, 606–614 (1988).
[11] I. Inbar and R. E. Cohen, Phys. Rev. B **53**, 1193 (1996).
[12] Y. Watanabe, T. Sota, K. Suzuki, N. Iyi, K. Kitamura, and S. Kimura, J. Phys.: Condens. Matter **7**, 3627 (1995).
[13] W. Zhang, Q. Cui, Y. Pan, S. Dong, J. Liu, and G. Zou, Chin. Phys. Lett. **19**, 1666–1672 (2002).
[14] A. Huanosta, E. Alvarez, M. E. Villafuerte-Castrejoń, and A. R. West, Mater. Res. Bull. **39**, 2229–2240 (2004).
[15] N. Tahiri, N. Masaif, and A. Jennane, J. Mater. Environ. Sci. **3**, 226–231 (2012).
[16] S. Xiang, L. Liu, J. Zhao, X. Zhou, Q. Jin, Y. Zhang, S. Liu, Z. Wang, Y. Bi, J. Xu, H. Geng, C. Dai, L. Cai, Q. Qu, J. Liu, C. Wang, and X. Zhang, J. Phys.: Condens. Matter **25**, 215401 (2013).
[17] M. Nakamuraa, S. Takekawa, and Y. K. Furukawa, J. Cryst. Growth **245**, 267–272 (2002).
[18] H. K. Mao, J. Xu, and P. M. Bell, J. Geophys. Res. **91**, 4673–4676, doi:10.1029/JB091iB05p04673 (1986).
[19] G. J. Piermarini, S. Blook, J. D. Barnett, and R. A. Forman, J. Appl. Phys. **46**, 2774–2780 (1975).
[20] F. Izumi and T. Ikeda, Mater. Sci. Forum **321–324**, 198–205 (2000).
[21] T. Yamanaka, T. Fukuda, T. Hattori, and H. Sumiya, Rev. Sci. Instrum. **72**, 1458–1462 (2001).
[22] S. Sasaki and K. Tsukimura, J. Phys. Soc. Jpn. **56**, 437–440 (1987).
[23] T. Yamanaka, T. Okada, and Y. Nakamoto, Phys. Rev. B **80**, 094108 (2009).
[24] T. Hahn, International Tables for Crystallography (Springer, Dordrecht, The Netherlands, 2005), Vol. A.
[25] P. Coppens, T. N. Guru Row, P. Leung, E. D. Stevens, P. J. Becker, and Y. W. Yang, Acta Cryst. A **35**, 63–72 (1979).
[26] R. J. van der Wal and R. F. Stewart, Acta Cryst. A **40**, 587–593 (1984).
[27] T. Yamanaka, T. Fukuda, Y. Komatsu, and H. Sumiya, J. Phys.: Condens. Matter **14**, 10545–10551 (2002).
[28] R. D. Shannon, Acta Cryst. A **32**, 751–767 (1976).
[29] V. Goplan and M. C. Gupta, Appl. Phys. Lett. **68**, 888–890 (1996).
[30] T. Yamanaka, Y. Komatsu, and H. Nomori, Phys. Chem. Min. **34**, 307–318 (2007).
[31] F. Birch, Phys. Rev. **71**, 809–824 (1947).
[32] J. A. Sanjurjo, E. L. Cruz, and G. Burns, Phys. Rev. B **28**, 7260 (1983).
[33] M. Ahart, R. E. Cohen, R. J. Hemley, S. Sinogeikin, O. Shebanova, D. Ikuta, and Z. G. Ye, Phys. Rev. B **86**, 224111 (2012).
[34] B. Chaabane, J. Kreisel, P. Bouvier, G. Lucazeau, and B. Dkhil, Phys. Rev. B **70**, 134114 (2004).
[35] M. Ahart, R. E. Cohen, V. Struzhkin, E. Gregoryanz, D. Rytz, S. Prosandeev, R. J. Hemley, and H. K. Mao, Phys. Rev. B **71**, 144102 (2005).